Ligand ordering determines the catalytic response of hybrid palladium nanoparticles in hydrogenation†

Davide Albani,‡[a] Gianvito Vilé,‡[a] Sharon Mitchell,[a] Peter T. Witte,[b] Neyvis Almora-Barrios,[c] René Verel,[a] Núria López*[c] and Javier Pérez-Ramírez*[a]

Supported palladium nanoparticles, prepared by reducing the active metal in the presence of the hexadecyl(2-hydroxyethyl)dimethylammonium dihydrogen-phosphate (HHDMA) ligand and depositing the resulting colloids on titanium silicate ($TiSi_2O_6$), represent a proven alternative to the archetypal poisoned catalysts in industrially-relevant selective hydrogenations. To date, a key aspect in the design of these hybrid nanocatalysts remains unaddressed, namely the impact of the ligand content on the catalytic behaviour. In order to assess the structural and associated catalytic implications of this variable, we have prepared a series of Pd-HHDMA/$TiSi_2O_6$ catalysts with different HHDMA content (0.3–16.8 wt%), keeping the average particle size (5 nm) and Pd content (0.3 wt%) constant. The materials are characterised with a toolbox of methods, including advanced microscopy and solid-state nuclear magnetic resonance, in order to assess the structure metal–ligand interface and the mobility of the alkyl chain. Continuous-flow three-phase hydrogenations of short-chain acetylenic compounds, nitriles, and carbonyls reveal an increase in the catalytic activity with the ligand content. Density Functional Theory indicates that the ligand behaves as a self-assembled monolayer, changing its adsorption configuration as a function of the HHDMA concentration. At low coverage, the organic layer lies almost flat on the surface of the metal nanoparticle blocking a large number of metal sites and resembling a two-dimensional catalyst; high HHDMA coverages favour an extended three-dimensional configuration of the alkyl chain, and consequently a lower fraction of Pd sites are poisoned. These results provide new fundamental insights into the role of the ligand on the catalytic activity and can enable the design of hybrid nanocatalysts with optimised performance.

Introduction

Nanostructured materials combining both inorganic and organic functionalities find increasing applications as heterogeneous catalysts[1,2] due to the unique properties that result from complementary interactions at the inorganic–organic interface.[3–6] These materials are typically prepared by liquid-phase reduction–deposition techniques, in which the metal precursor is first reduced in the presence of an organic ligand to form colloidal metal nanoparticles, that are subsequently deposited on a suitable support. Under the appropriate conditions, it is possible to obtain metal crystallites of variable particle size and shape.[3–6] However, these synthetic methods have crucial disadvantages (*i.e.*, the need for low-boiling point organic solvents, the fast addition of expensive or toxic reductants) that have long hampered their industrial exploitation.[8] The identification of hexadecyl-2-hydroxyethyl-dimethyl ammonium dihydrogen phosphate (HHDMA) as a ligand that combines both reducing and stabilising functionalities in a single, water-soluble molecule, has recently enabled the synthesis at industrial level of colloidally-prepared Pd, Pt, and Pd–Pt nanoparticles supported on inert carriers such as titanium silicate ($TiSi_2O_6$) and activated carbon.[7,8] The versatility of this new generation of catalysts has been demonstrated for the selective hydrogenation of functionalised alkynes and nitroaromatics,[9–11] primary reactions in the fine chemical and pharmaceutical industries for the manufacture of polymers, vitamins, agrochemicals, and fragrances.[12]

Kinetic tests in flow mode, in-depth characterisation, and Density Functional Theory (DFT) calculations have

[a] *Institute for Chemical and Bioengineering, Department of Chemistry and Applied Biosciences, ETH Zurich, Vladimir-Prelog-Weg 1, 8093 Zurich, Switzerland. E-mail: jpr@chem.ethz.ch*
[b] *BASF Nederland BV, Strijkviertel 67, 3454PK De Meern, The Netherlands*
[c] *Institute of Chemical Research of Catalonia (ICIQ) and Barcelona Institute of Technology (BIST), Av. Països Catalans 16, 43007 Tarragona, Spain. E-mail: nlopez@iciq.es*

† Electronic supplementary information (ESI) available. The material contains additional characterisation and catalytic data and theoretical results. See DOI: 10.1039/c5cy01921d

‡ These authors contributed equally to the work.

significantly contributed to the structural understanding of these materials, showing that the ligand shell is a main player in determining their efficient and selective catalytic behaviour. Despite the pioneering work of Schwartz and co-workers[13] on the effect of the ligand concentration and performance of thiol-based materials, those results cannot be extrapolated to much more complex ligands composed of multiple chemical units. In fact, a literature analysis concluded that these points have not yet been addressed. Our contribution accomplishes all the challenges faced in the controlled synthesis of Pd-HHDMA/$TiSi_2O_6$ catalysts with variable ligand content, but equivalent metal concentration (0.3 wt%) and average particle size (5 nm), in the characterisation of the ligand organisation and in the rationalisation of its catalytic impact of these tasks, demonstrating the critical and nontrivial impact of ligand ordering. Catalytic tests were conducted in a continuous-flow three-phase micro-reactor, showing an increased catalytic activity with increasing ligand concentration for the hydrogenation of alkynes, nitriles, and carbonyls. DFT calculations and electron microscopy provide fundamental insights into this counterintuitive structure–performance relationship, which is explained based on the relative assembly of ligands on the nanoparticle surface.

Experimental

Catalyst preparation

Hybrid palladium nanocatalysts with different ligand content (0.3–16.8 wt%) were synthesised by reduction–deposition, using HHDMA as the stabiliser. The materials are coded as Pd-HHDMA-*n*, where n = 1–4 and represents the relative ligand concentration (see Table 1). As depicted in Fig. 1, an aqueous solution of HHDMA (100 cm^3, 30%) was diluted in deionised water (3000 cm^3) and mixed with an aqueous solution of Na_2PdCl_4 (0.1 M, 50 cm^3). The pH of the mixture was adjusted to 5 by the dropwise addition of NaOH (12 M). The resulting solution, which contains 0.38 mg Pd cm^{-3}, was heated to 358 K and stirred at this temperature for 2 h to form the colloids, obtaining metal nanoparticles of approximately 5 nm. Note that, the metal particle size is solely controlled by the addition of HHDMA in the initial solution. For the preparation of Pd-HHDMA-3 and Pd-HHDMA-4, titanium silicate (30 or 40 g, respectively) was added to a defined amount of colloidal suspension (200 or 600 cm^3, respectively) and stirred for 1 h. The mother liquor containing excess colloidal nanoparticles from the preparation of Pd-HHDMA-4 was divided into two equal portions and one of these portions was added to 27 g of $TiSi_2O_6$ and stirred for 1 h obtaining Pd-HHDMA-1. For the preparation of Pd-HHDMA-2, titanium silicate (10 g) was added to 300 cm^3 of colloidal suspension and stirred for 1 h. The resulting mother liquor was divided into two equal portions; titanium silicate (20 g) was added to one portion, and the resulting suspension was stirred for 1 h, obtaining Pd-HHDMA-2. Prior to use, the catalysts were separated by filtration and extensively washed with deionised water.

Catalyst characterisation

The palladium content in the supported catalysts was determined by inductively coupled plasma-optical emission spectrometry (ICP-OES) using a Horiba Ultra 2 instrument equipped with photomultiplier tube detection. The C, H, N, and P contents were determined by infrared spectroscopy using a LECO CHN-900 combustion furnace. Nitrogen isotherms were measured at 77 K in a Micrometrics ASAP 2020 instrument, after evacuation of the samples at 393 K for 6 h. Transmission electron microscopy (TEM) was undertaken using an FEI Talos S200 microscope operating at 200 kV with a 70 μm C2 aperture, 0.4 nA beam current. The colloidal samples were supported on continuous carbon-coated Cu grids and negatively stained with a 1 vol% aqueous uranyl acetate solution in order to increase the contrast between the ligand tail and the background. Images were recorded in low-dose mode to minimise radiation damage to the sample. The supported catalysts were dispersed as dry powders on lacey carbon coated copper grids. Scanning electron microscopy (SEM) was undertaken in an FEI Magellan 400 microscope working at 30 kV and 50 pA. The particle size distribution was assessed by counting more than 150 individual Pd nanoparticles. CO chemisorption was performed using a Thermo TPDRO 1100 unit. The samples were pre-treated *in situ* at 393 K under He flow (20 cm^3 min^{-1}) for 60 min, and reduced at 348 K under flowing 5 vol% H_2/He (20 cm^3 min^{-1}) for 30 min. Thus, 0.344 cm^3 of 1 vol% CO/He was pulsed over the catalyst bed at 308 K every 4 min. The palladium dispersion was calculated from the amount of chemisorbed CO, considering an atomic surface density of 1.26×10^{19} atoms m^{-2} and

Table 1 Characterisation data of the catalysts

Catalyst	Pd[a] (wt%)	C[a] (wt%)	H[a] (wt%)	N[a] (wt%)	P[a] (wt%)	HHDMA[a] (wt%)	C/Pd[b] (–)	Weight loss[c] (%)	S_{BET}[d] (m^2 g^{-1})	V_{pore}[e] (cm^3 g^{-1})	D_{CO}[f] (%)	D_{SEM}[g] (%)
Pd-HHDMA-1	0.3(0.3)[h]	0.2(0.3)	1.6(1.4)	0.01(0.03)	0.02(0.1)	0.3	1	4	426	0.30	23	24
Pd-HHDMA-2	0.3	2.5	1.8	0.13	0.02	4.3	9	8	330	0.21	22	23
Pd-HHDMA-3	0.3	4.8	2.1	0.23	0.03	8.2	15	10	273	0.20	13	22
Pd-HHDMA-4	0.3(0.3)	9.8(9.4)	2.7(2.7)	0.45(0.53)	0.06(0.12)	16.8	31	17	105	0.07	11	24

[a] Elemental analysis. [b] Weight ratio. [c] Thermogravimetric analysis. [d] BET method. [e] Volume of N_2 at p/p_0 = 0.95. [f] CO chemisorption. [g] Scanning electron microscopy. [h] Elemental analysis of the catalyst after hydrogenation. Conditions: W_{cat} = 0.2 g, T = 343 K, P = 10 bar, F_L (benzaldehyde + methanol) = 1 cm^3 min^1, and $F_G(H_2)$ = 48 cm^3 min^{-1}.

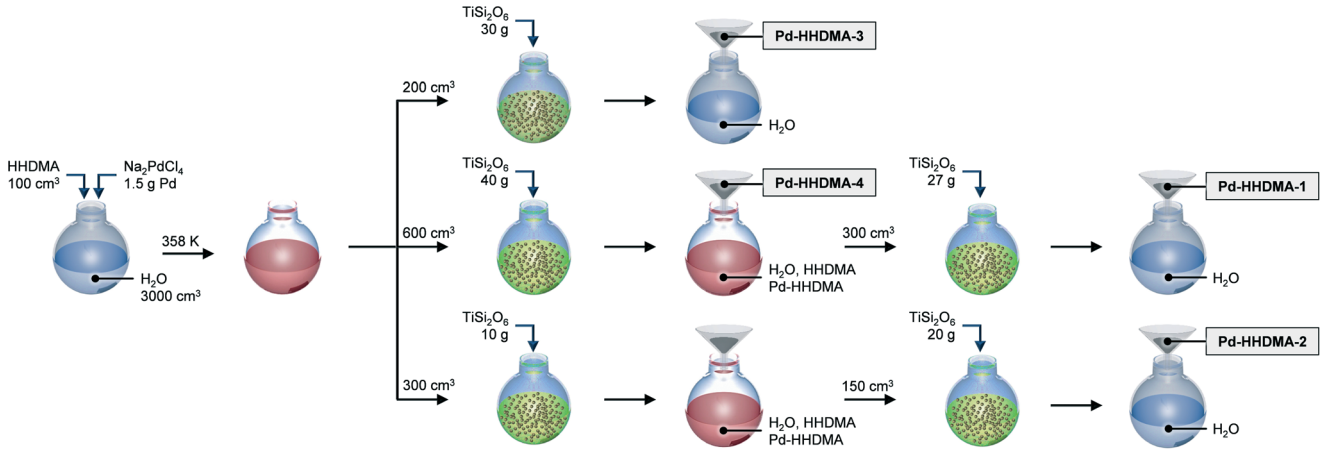

Fig. 1 Schematic illustration of the synthetic steps involved in the preparation of the supported catalysts.

an adsorption stoichiometry of Pd/CO = 2. The stoichiometry is the most suited for chemisorption measurements conducted over palladium catalysts at room temperature and in dynamic mode.[14] X-ray photoelectron spectroscopy (XPS) was measured in a Physical Electronics Instruments Quantum 2000 spectrometer using monochromatic Al Kα radiation generated from an electron beam operated at 15 kV and 32.3 W. The spectra were collected under ultra-high vacuum conditions (residual pressure = 5×10^{-8} Pa) at a pass energy of 50 eV. All binding energies were referenced to that of C 1s at 288.2 eV in order to compensate for charging effects. Thermogravimetric analysis was performed in a Mettler Toledo TGA/DSC 1 Star system. Prior to measurement, the samples were dried in N_2 (40 cm^3 min^{-1}) at 393 K for 1 h. The analysis was performed in air (40 cm^3 min^{-1}), heating the sample from 298 K to 1173 K at a rate of 5 K min^{-1}. ^{13}C, ^{1}H, and ^{31}P magic angle spinning nuclear magnetic resonance spectra were recorded on a Bruker AVANCE III HD NMR spectrometer at a magnetic field of 16.4 T corresponding to a ^{1}H Larmor frequency of 700.13 MHz. A 4 mm double resonance probe head at a spinning speed of 10 kHz was used for all experiments. The ^{13}C spectra were acquired using a cross polarization experiment with a contact time of 2 ms and a recycle delay of 1 s. A total of 64×10^3 scans were added for each sample. The ^{31}P experiments used a single pulse excitation sequence with a recycle delay of 1 s. Between 39×10^3 and 96×10^3 scans were acquired depending on the sample. Both ^{13}C and ^{31}P experiments used high-power ^{1}H decoupling during acquisition using a SPINAL-64 sequence.[15]

Catalyst evaluation

The hydrogenation of 1-hexyne (Acros Organics, 98%), 2-methyl-3-butyn-2-ol (Acros Organics, 99.9%), 3-hexyne (Acros Organics, 99%), 4-octyne (Acros Organics, 99%), benzonitrile (TCI, 99%), and benzaldehyde (Fluka, 99%) was carried out in a fully-automated flooded-bed micro-reactor (ThalesNano H-Cube Pro™), in which the gaseous hydrogen produced *in situ* and the liquid reactant flow concurrently upward through a fixed-bed reactor (3.5 mm i.d.) with catalyst particles of 0.2–0.4 mm. For the hydrogenation of alkynes, the catalyst (0.10 g) was diluted with titanium silicate (0.12 g, Aldrich, 99.8%). For the hydrogenation of nitriles and carbonyls, the undiluted catalyst (0.2 g) was used. The liquid feed contained 5 vol% of substrate and toluene (Fischer Chemicals, 99.95%), cyclohexane (Sigma-Aldrich, 99%), or methanol (Sigma-Aldrich, 99%) as solvents. The reactions were conducted at various temperatures (303–363 K), total pressures (1–40 bar), and liquid (0.3–1 cm^3 min^{-1}) and H_2 (36–48 cm^3 min^{-1}) flow rates. The reaction products were collected employing a liquid handler (Gilson GX-271), after 10–15 min of steady-state operation, and analysed offline using a gas chromatograph (HP-6890) equipped with a HP-5 capillary column and a flame ionisation detector. The hydrogenation of 3-hexyn-1-ol was conducted in batch mode using a 250 cm^3 stainless-steel autoclave. The reactor was charged with catalyst (0.4 g) and 100 g of a solution of 3-hexyn-1-ol in ethanol (4.5 wt%). The autoclave was flushed with hydrogen and pressurised with 3 bar of hydrogen. The conversion (X) of a given substrate was determined as the amount of reacted substrate divided by the amount of substrate at the reactor inlet. The selectivity (S) to each product was quantified as the amount of the particular product divided by the amount of reacted substrate. The reaction rate (r) was expressed as the number of moles of product per mole of Pd and unit time.

Computational details

Density Functional Theory (DFT) calculations were performed using the Vienna *ab initio* Simulation Package (VASP),[16–18] employing the generalised gradient approximation with the revised Perdew–Burke–Ernzerhof exchange–correlation functional.[19] The interaction between the valence electrons and the core was described with the projected augmented wave method in the implementation of Kresse and Joubert.[18] A kinetic cut-off energy of 450 eV was used for the plane wave expansion of the wave functions. Due to the size of the

simulation cell (the shortest cell vector is *ca.* 28 Å), during ion relaxations, the reciprocal space integration was performed by considering only the Γ-point of the Brillouin zone. The van der Waals contributions were described elsewhere, using the semi-empirical DFT-D2 (ref. 20) approach and the parameters optimised for this metal.[21] The palladium (111) surface was simulated using periodic slabs with a thickness of five layers, which were separated from the neighbour by a vacuum gap of 20 Å to provide sufficient space for the adsorbates, avoiding in this way potentials interactions with neighbouring (periodic image) slabs. In a large $p(10 \times 10)$ unit cell, 5, 10, 18 and 25 HHDMA chains were adsorbed on the surface, obtaining coverages of 0.5, 0.10, 0.18, 0.25 monolayers (ML). In particular, the structures with lower HHDMA content were obtained by using the fully saturated surface as the initial step, and removing a certain fraction of ligand. Prior to performing DFT-D2 calculation, the different configurations were equilibrated using the classic molecular dynamics (MD) simulations. The MD simulation allows the HHDMA chains to relax fast and occupy the empty volume of the missing ligands. The DFT-D2 methodology included all the required interactions: electrostatic (between the ions in the ligand and the metal), covalent (anion–metal), and van der Waals (between the metal and the ligand, and between the ligand tails). Since the ligand interacts both with the metal surface and with the organic tail of neighbouring ligands, the dominant interactions depend on the coverage. At low concentrations, van der Waals forces between the surface and the aliphatic chains are prevalent. As the ligand concentration increases, the electrostatic interaction between the phosphate ion of the ligand and the metal dominates over both the metal–alkyl chain interaction (−0.05 eV per CH_2 group),[22] and that between the alkyl chains and the solvent. The optimised layers are not completely ordered and, thus, an average measure of their orientation with respect to the surface is required. This dynamic behaviour of the carbon atoms tail of the HHDMA molecules can be characterised by an order parameter, S_{HHDMA}, which measures the average orientational order of each methylene chain segment within the hydrocarbon tail (details in the ESI†). The order parameter is defined as $S_{HHDMA} = 0.5 \langle 3\cos\theta_i \cos\theta_j - \delta_{ij} \rangle$, where θ_i (θ_j) is the angle formed between the ith (jth) molecular axis and the normal to the surface and δ_{ij} is the Kronecker delta function.[23] The order parameter is finally averaged over the number of ligand molecules in the simulation box. To reduce the calculation time, we have only averaged the latter over the chains resulting from the DFT-D2 optimised structure. To evaluate the influence of the ligand content on the activity and selectivity in the hydrogenation of alkynes, we have calculated the adsorption energy, E_{ads}, of specific reactant, product, and solvent (*i.e.*, 1-hexyne, 1-hexene and toluene) on the Pd-$(HHDMA)_x$ materials. Adsorption energies were found using the equation: $E_{ads} = E_{Pd\text{-}(HHDMA)x\text{-}molecule} - (E_{Pd\text{-}(HHDMA)x} + E_{molecule})$, where $E_{Pd\text{-}(HHDMA)x\text{-}molecule}$ is the energy of the complete system including the metal, the HHDMA molecules, and the adsorbate; $E_{Pd\text{-}(HHDMA)x}$ is the energy of the same system in the absence of the adsorbate; and $E_{molecule}$ is the energy of the isolated gas-phase molecule.

Results and discussion

Catalyst characterisation

To assess the effects exerted by the HHDMA ligand on the catalytic performance, four catalysts have been synthesised with equivalent Pd loading (0.3 wt%), but different ligand content. Table 1 shows the bulk composition and morphological characteristics of the resulting materials. Elemental analysis of C, H, N, and P confirms the increasing ligand content of the catalysts from Pd-HHDMA-1 to Pd-HHDMA-4.

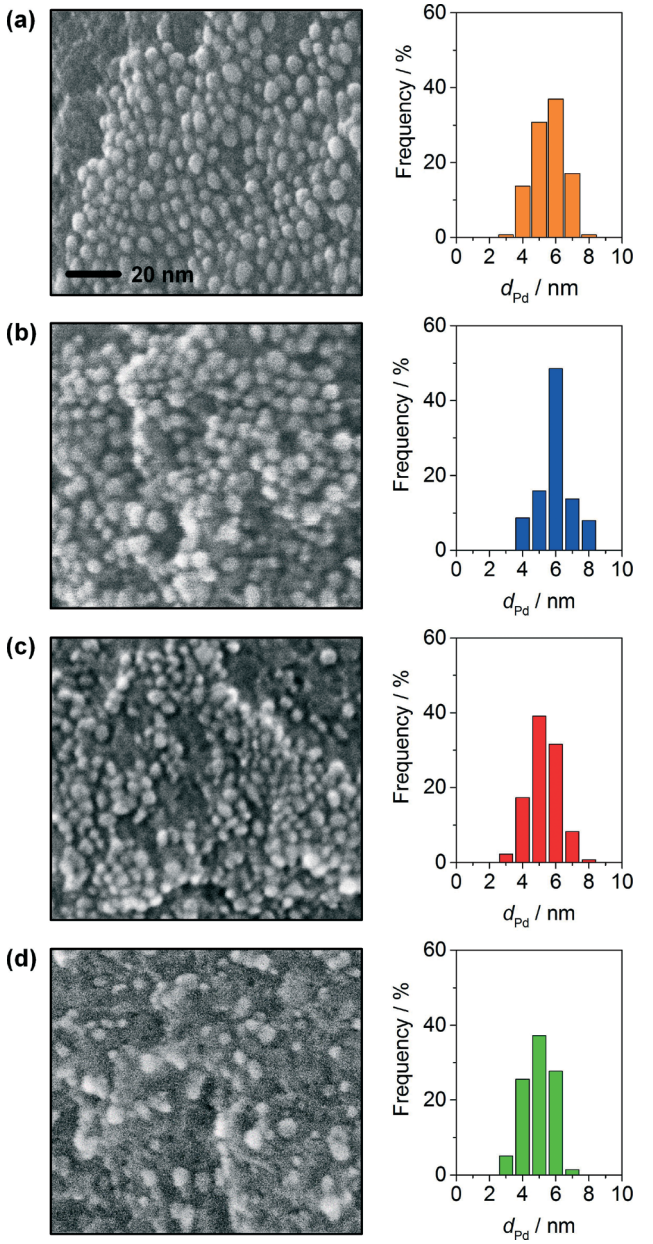

Fig. 2 Scanning electron micrographs and particle size distributions of Pd-HHDMA-1 (a), Pd-HHDMA-2 (b), Pd-HHDMA-3 (c), Pd-HHDMA-4 (d). The scale bar in (a) applies to all micrographs.

Inspection of the scanning electron micrographs reveals that the palladium nanoparticles possess a uniform spherical shape (Fig. 2). Estimation by image analysis evidences an average particle diameter of around 5 nm (Fig. 2). The particles are unevenly distributed over the surface of the support, appearing to be self-assembled into islands in certain regions. However no evidence of particle agglomeration is observed despite the high concentration of Pd in the samples. This can be related to the function of the ligand shell in separating the metal phase during synthesis. XPS spectra show in all cases a single Pd $3d_{5/2}$ core level peak at 335.3 eV assigned to Pd^0, confirming that the palladium surface is fully metallic, independent of the amount of HHDMA available and corresponding reducing capability (Fig. S1†).

To determine the thermal stability of the ligand shell, thermogravimetric analyses in air were conducted (Fig. 3). In all cases, the ligand decomposition started at 500–550 K, and the relative weight loss was consistent with the ligand content derived from C, H, and N analysis (Table 1). The impact of the ligand content on the metal dispersion was examined by CO chemisorption a technique that has been also applied in the past to probe the number of free Pd sites available for catalysis in Pd-HHDMA/$TiSi_2O_6$, Pd-HHDMA/C, and Pt-HHDMA/C.[9,10] Consistent with the relative amount of organic moiety, the maximum degree of dispersion (23%) is evidenced in Pd-HHDMA-1 and decreases to 11% in Pd-HHDMA-4. It should be noted that this trend cannot be predicted based on the examination of the metal size distribution alone, from which negligible differences are evidenced between samples. Similarly, the sample exhibiting the highest ligand content (Pd-HHDMA-4) displays a surface area (105 $m^2\ g^{-1}$), four times smaller than that of the catalyst with the lowest one (426 $m^2\ g^{-1}$, Table 1). This is attributed to the presence of HHDMA ligand on both the metal nanoparticle and surface of the titanium silicate support. We have tried to determine how the ligand distributes between the metal and the carrier, employing thermogravimetric analysis (based on the possible different decomposition patterns for HHDMA attached to the support and to the metal), and nuclear magnetic resonance spectroscopy (based on the local environment experienced by the ligand on the metal and on the support). In both case, we have not been able to conclusively quantify the amount of ligand per nanoparticle because of the absence of differences in the patterns. Besides, the C : P and C : N values could not be used to obtain a preliminary estimation of the separation of the ligand. In fact, by comparing the atomic C : P and C : N ratios (*i.e.*, 422 and 25, respectively, for Pd-HHDMA-4) with the theoretical values based on the HHDMA stoichiometry (C : P = 20 and C : N = 20), a discrepancy is found. A published paper[8] hypothesised that this can be attributed to the fact that HHDMA ligand binds on the $TiSi_2O_6$ by the amino group, releasing orthophosphoric acid. This hypothesis, however, still needs to be supported experimentally. In this context, our preliminary results indicate that the adsorption configuration of the ligand on the carrier is much more complex, since we have detected P-containing species by elemental mapping in areas where metal nanoparticles are not present. For this reason, we believe that HHDMA adsorbs on the support in different configurations, with and without the orthophosphate group. As a consequence, all the correlations derived in this manuscript have always been referred to the total ligand content in the catalyst. The samples were further characterised by solid-state ^{13}C and ^{31}P MAS-NMR. The peaks in the ^{13}C MAS NMR spectra (Fig. 4a) can be assigned in analogy with the signals observed in the solution state NMR spectra. In particular, the peaks above 40 ppm all originate from carbon positions in close proximity to the nitrogen. At the same time, these resonances display a markedly increased linewidth when compared to many of the peaks below 40 ppm which mainly correspond to positions in the aliphatic tail of the molecule.

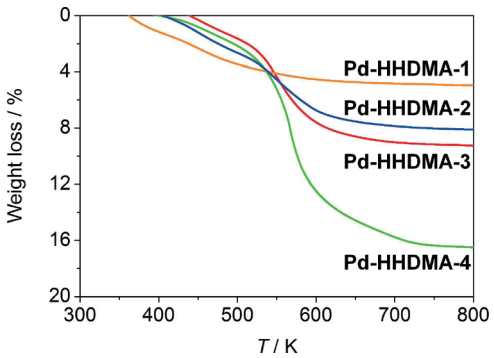

Fig. 3 Thermogravimetric profiles of the catalysts.

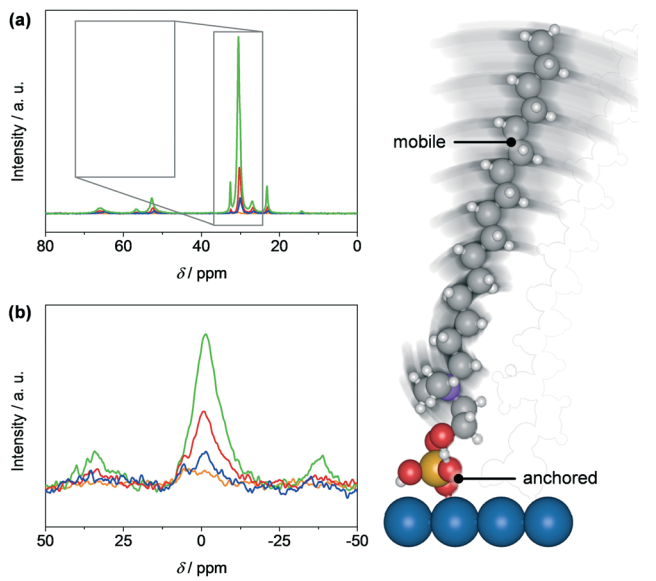

Fig. 4 ^{13}C (a) and ^{31}P (b) magic-angle spinning nuclear magnetic resonance spectroscopy of Pd-HHDMA-1 (orange), Pd-HHDMA-2 (blue), Pd-HHDMA-3 (red), Pd-HHDMA-4 (green). The picture on the right side depicts the mobile character of the ligand tail and the rigidity of the phosphate group. Colour codes: Pd (blue), P (yellow), O (red), C (light grey), and N (purple).

We interpret this as being indicative of a difference in mobility (on the NMR timescale) between the head-group and the tail, where presumably the aliphatic tail is dynamic and the signals in the NMR spectra are motionally narrowed. Contrarily, the ^{31}P MAS NMR spectra (Fig. 4b) display only a single, broad isotropic signal around 0 ppm, which is consistent with an orthophosphate anion. This peak is flanked on either side by a spinning sideband giving a rough estimate of the chemical shift anisotropy of about 50 ppm. The ^{31}P peak with a full width half height of approximately 2 kHz seems to be inhomogeneous in nature and is indicative of a statically disordered environment. Overall, the broadness of the peak in the ^{31}P signal compared to the sharp signals observed in the ^{13}C spectra reflect the more rigid bonding of the orthophosphate anion with respect to the ligand tail, which exhibits a high degree of structural flexibility.

Hydrogenation of alkynes

The performance of the catalysts containing variable ligand concentration was assessed in the hydrogenation of 1-hexyne (Fig. 5). In general, the activity of the materials clearly increases with the amount of HHDMA in the catalyst. For example, the rate of 1-hexyne conversion at 363 K and 1 bar is 1.1×10^3 h^{-1} over Pd-HHDMA-1, 1.8×10^3 h^{-1} over Pd-HHDMA-2, 2.5×10^3 h^{-1} over Pd-HHDMA-3, and 2.9×10^3 h^{-1} over Pd-HHDMA-4, a value which is 2.5 times higher activity than that for Pd-HHDMA-1. The improved activity with the total ligand concentration is confirmed in the hydrogenation of 3-hexyne, 2-methyl-3-butyn-2-ol, and 4-octyne (Fig. 6, S2 and S3†), as well as for the hydrogenation of 1-hexyne using cyclohexane instead of toluene as a solvent (Fig. S4†). This trend, which appears to contrast with the fact that the number of free atoms determined by CO chemisorption is reduced upon increasing of the HHDMA content, is explained below. In terms of alkene selectivity, it is noteworthy to highlight that the catalysts can only be compared at moderate and similar degree of conversion (*ca.* 30%). This can facilitate the detection of deactivation phenomena (which in turn are somewhat obscure when catalytic tests are undertaken in a batch reactor, reaching high degree of alkyne conversion). In the window of temperatures and pressures where these catalysts are applied industrially ($T < 323$ K and $P < 2$ bar), the alkene selectivity approaches 100%. Particularly, for the hydrogenation of 1-hexyne at 363 K and 1 bar, the selectivity to 1-hexene is 100% over Pd-HHDMA-1 and Pd-HHDMA-2, 96% over Pd-HHDMA-3 (4% alkane), and 90% over Pd-HHDMA-4 (5% alkane, 5% 2-hexene). The result can be generalised for the hydrogenation of 3-hexyne, 2-methyl-3-butyn-2-ol, and 4-octyne (Fig. 6, S2 and S3†). In all cases, a slight decrease in alkene selectivity is observed at high temperatures and pressures ($T > 343$ K and $P > 3$ bar). This, however, is expected for any modified palladium catalyst and is related to the tendency of palladium to form of α and β-hydrides, catalysing isomerisation and over-hydrogenation reactions.[24]

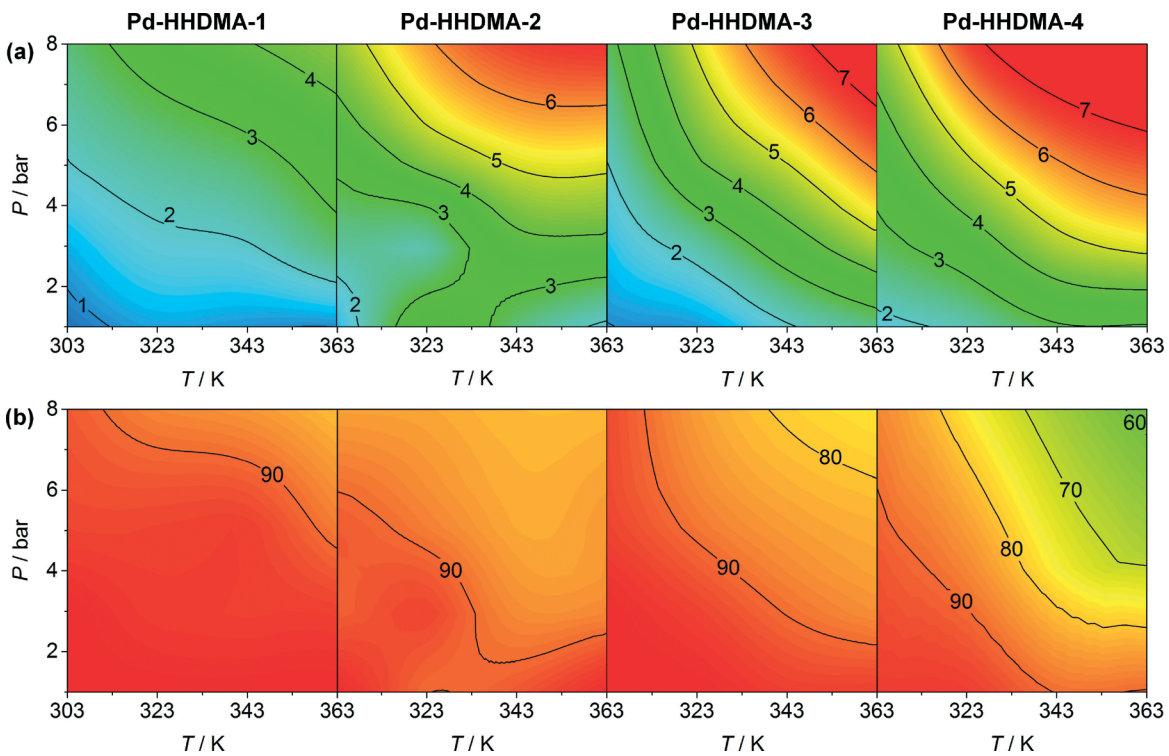

Fig. 5 Reaction rate (in 10^3 h^{-1}, a) and selectivity to 1-hexene (in %, b) in the hydrogenation of 1-hexyne. Conditions: W_{cat} = 0.1 g, F_L (1-hexyne + toluene) = 1 cm^3 min^{-1}, and $F_G(H_2)$ = 36 cm^3 min^{-1}. The contour maps were obtained through spline interpolation of 16 experimental points.

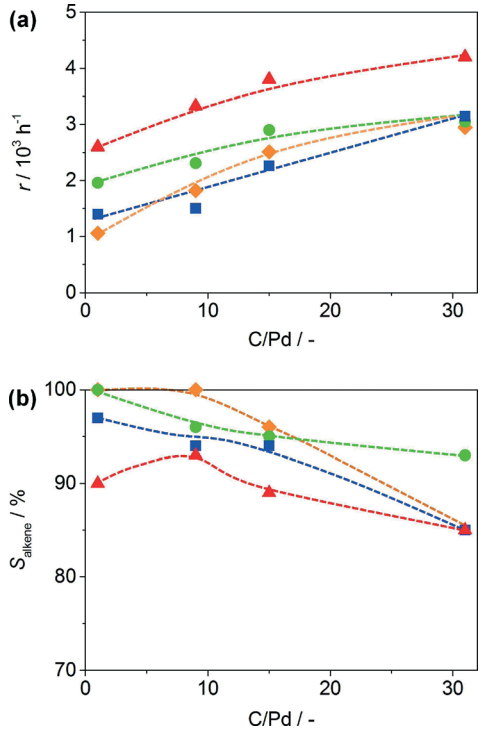

Fig. 6 Rate of reaction (a) and selectivity to the desired product (b) *versus* the total ligand content (C/Pd) in the hydrogenation of 1-hexyne (orange), 3-hexyne (green), 2-methyl-3-butyn-2-ol (blue), and 4-octyne (red). Conditions: W_{cat} = 0.1 g, T = 363 K, P = 1 bar, F_L (1-hexyne + toluene) = 1 cm^3 min^{-1}, and $F_G(H_2)$ = 36 cm^3 min^{-1}.

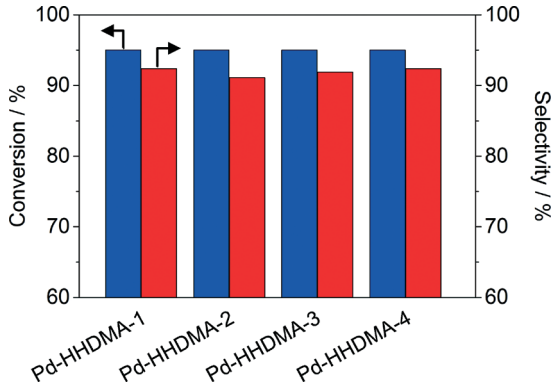

Fig. 7 Conversion and selectivity to cis-3-hexen-1-ol in the batch semi-hydrogenation of 3-hexyn-1-ol. Conditions: W_{cat} = 0.4 g, T = 303 K, p (H_2) = 3 bar, t = 10–15 min.

To study the activity of these materials at high conversion levels, the hydrogenation of 3-hexyn-1-ol was investigated in batch mode (Fig. 7 and S7†). The batch experiments demonstrate that, at 95% of alkyne conversion, the alkene selectivity is approximately 90% over all samples, confirming the outstanding performance of the ligand-modified materials.

To demonstrate the robustness of the catalytic system, characterisation of the used Pd-HHDMA-1 and Pd-HHDMA-4 has been carried out. The Pd and HHDMA contents in the used catalysts are retained upon hydrogenation (Table 1), highlighting the absence of any leaching upon reaction.

Structure–performance relationships

In order to rationalise the catalytic performance of these materials, we have investigated the structure and organisation of the ligand interface, firstly through microscopy analyses. The direct observation of the hybrid nanocatalyst has often been approached by SEM and TEM.[4–8] However, the use of these conventional techniques is not straightforward due to both the low contrast of the organic layer and the structural changes which may occur upon irradiation. Without special care to preserve the structure and enhance the visibility of the organic shell, these techniques only provide information about the size of the metal core. More recent developments, particularly related to the study of biological materials, have permitted to employ low irradiation doses, dedicated supporting or staining strategies, and/or cryogenic conditions, to greatly extend the scope of modern microscopy techniques for the characterisation of organic–inorganic composites.[25] An advanced microscopic evaluation of this industrially-relevant catalyst can provide new fundamental insights on the properties of HHDMA-modified catalysts at the nanoscale, ultimately guiding the design of better hybrid catalyst. For this reason, we have analysed the free colloidal solution obtained before or during synthesis of the supported nanoparticles (Fig. 1). The micrographs in Fig. 8 depict the capping role of the ligand; the lighter circles corresponding to the HHDMA surfactant tail surround the dark spots in the centre to the Pd nanoparticles (as illustrated in the coloured inset). From the microscopy results, it appears that the average ligand thickness on the nanoparticles increases with the ligand content. The thickness of the ligand shell, in particular, passes from being barely visible (*ca.* 0–0.5 nm) in Pd-HHDMA-1 to 2.5 nm in Pd-HHDMA-3 (Fig. 8).

To assess the origins of the different thickness of the organic shell in the materials, it is important to estimate the average orientation of the ligand chain. For this reason, we introduce the order parameter, S_{HHDMA}, which in quantum chemistry measures the average orientational order of the methylene chain units within the hydrocarbon tail.[23] This concept describes the correlation between the structure of a self-assembled monolayer (SAM) and the metal and is defined as $S_{HHDMA} = 0.5 <3\cos\theta_i\cos\theta_j - \delta_{ij}>$, where θ_i is the angle between the ith molecular axis and the surface normal; θ_j is the angle between the jth molecular axis and the normal to the surface; and δ_{ij} is the Kronecker delta function. Notice, that the order parameter reaches a value of 0 when the surfactants flatten on the surface. At the maximal HHDMA density, a saturation value of $S_{HHDMA,max} = 1.24$ is obtained, corresponding to an angle of the self-assembled layer with respect to the normal to the surface of 34°. In general, Pd-HHDMA nanoparticles with a low ligand content present very low order parameters, S_{HHDMA}. This indicates that the chains are almost flattened on the surface. From the combined MD/

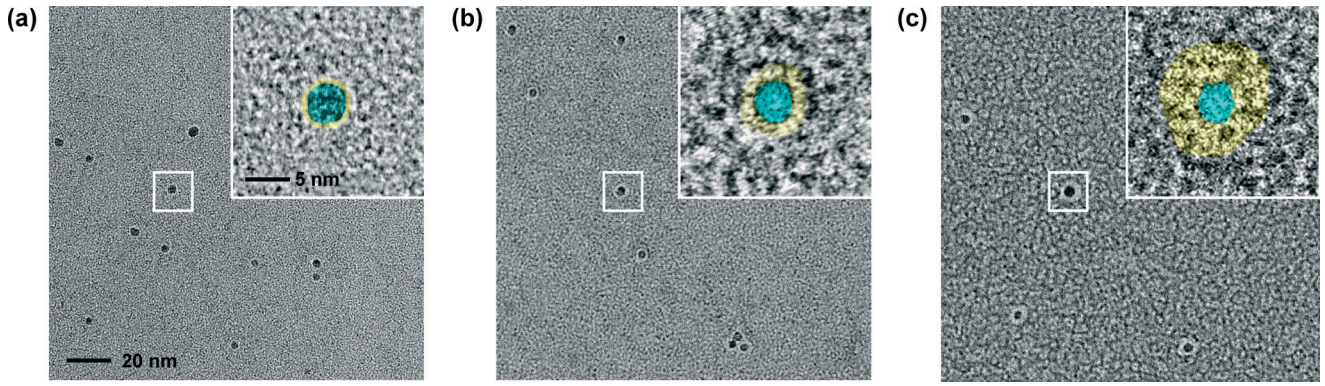

Fig. 8 Transmission electron micrographs of the colloidal Pd nanoparticles with different ligand content employed in the synthesis of Pd-HHDMA-1 (a), Pd-HHDMA-2 (b), and Pd-HHDMA-3 (c). The insets present a 4-fold magnification zoom of the boxed particles (light blue = palladium, yellow = HHDMA layer). The scale bars in (a) apply to all micrographs.

DFT-D2 calculations (see the ESI† for details), we have observed that this catalyst has a 2D-type surface, leaving small areas where non-poisoned Pd atoms can catalyse the reaction (Fig. 9a). This resembles the structure of the typical Lindlar catalyst (Fig. 10).[27] When the concentration of HHDMA increases, S_{HHDMA} also increases and the aliphatic chains assume a more extended configuration (exhibiting similar behaviour to a typical self-assembled monolayer), giving rise to a 3D-like material (Fig. 9a).[26] In this configuration, the organic shell moves cooperatively, opening channels in the structure where adsorption and reaction can occur. By correlating the hydrogenation rate with the order parameter (Fig. 9b and c), a linear correlation is obtained. This relationship indicates that S_{HHDMA} is the intrinsic descriptor for activity the ligand-coated nanoparticles. As depicted in Fig. S6,† this linear dependence can be generalised to all other substrates in this work, although different slopes could be observed, depending on the specific interaction

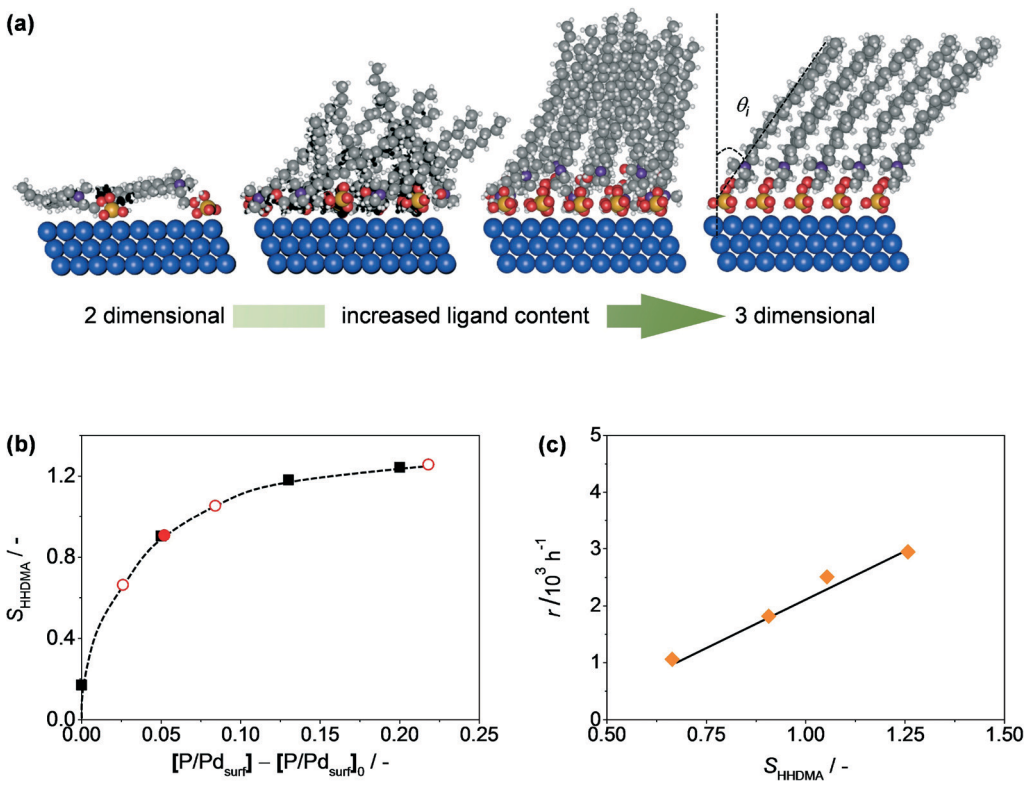

Fig. 9 Schematic representation of the catalysts structures with variable ligand concentration (a). Variation of the order parameter, S_{HHDMA}, as a function of the ligand content (b) and rate of 1-hexyne hydrogenation as a function of the order parameter (c). The red symbols in (b) represent experimental points and the black symbols refer to the theoretical data. Conditions: W_{cat} = 0.1 g, T = 363 K, P = 1 bar, F_L (1-hexyne + toluene) = 1 cm^3 min^{-1}, $F_G(H_2)$ = 36 cm^3 min^{-1}. Colour codes as in Fig. 4.

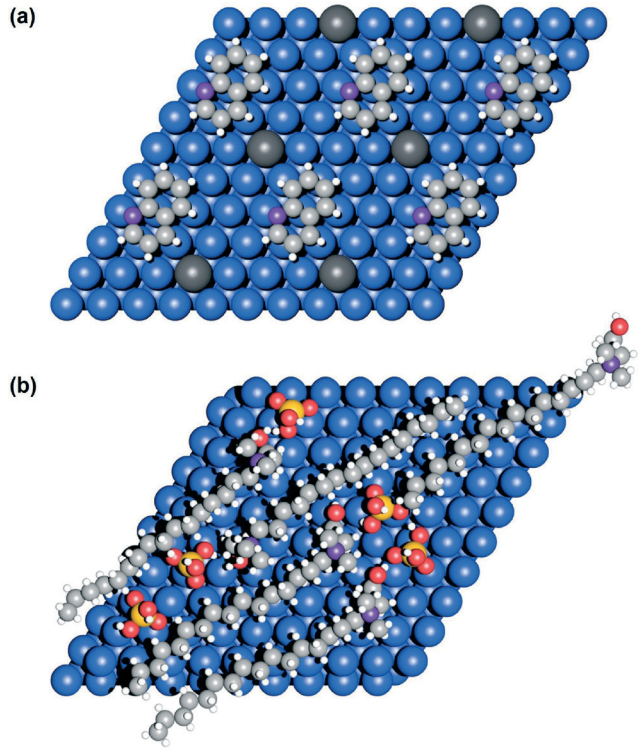

Fig. 10 Top view of the surface of the classical Lindlar catalyst poisoned with quinoline (a), and Pd-HHDMA-1 (b). Colour codes: Pd (blue), Pb (dark grey), P (yellow), O (red), C (light grey), and N (purple).

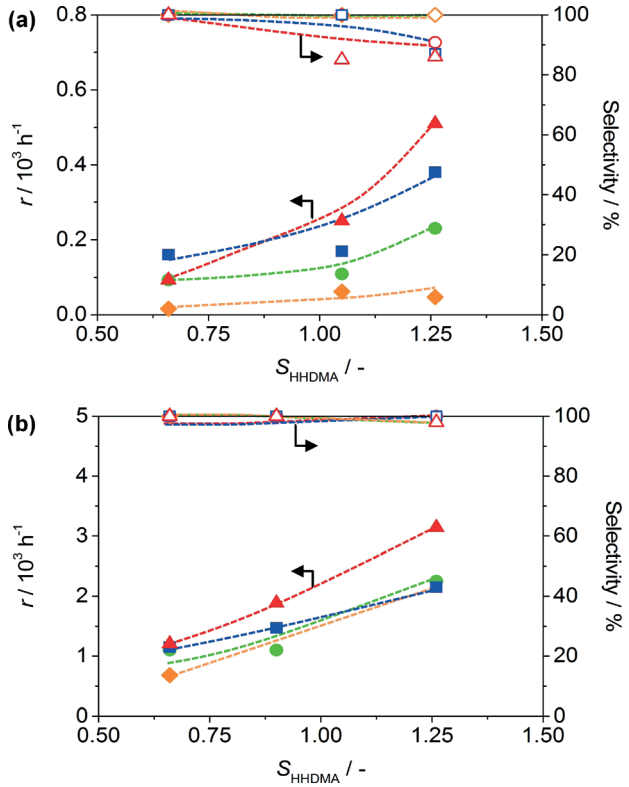

Fig. 11 Rate of reaction and selectivity *versus* the order parameter (S_{HHDMA}) in the hydrogenation of benzonitrile to benzylamine (a), and benzaldehyde to benzyl alcohol (b). T = 343 K (orange), 353 K (green), 363 K (blue), and 373 K (red). Other conditions: W_{cat} = 0.2 g, P = 40 bar (a) and 10 bar (b), F_L (substrate + methanol) = 0.3 cm^3 min^{-1} (a) and 1 cm^3 min^{-1} (b), and $F_G(H_2)$ = 48 cm^3 min^{-1}.

between the catalyst (metal and ligand) and the substrate. The activity trend observed in Fig. 5 and 11 could be in contrast with the fact that the number of free surface atoms required for the catalytic reaction decreases upon ligand coverage increase, as shown by the CO chemisorption values. This effect, however, can be rationalised by considering the different size of CO and the alkyne molecules. While CO can easily access the to the active site, even when the ligand is flattened on the surface, due to its small size, the adsorption of the bulkier reactants at low ligand content is less favourable. This results in the atypical catalytic trend observed, with high activity only at high HHDMA content, when 'free' pockets on the surface are orderly formed and are accessible to bulky acetylenic compounds.

The variation in selectivity over the densely-packed HHDMA ligands at high coverage also arises from a combination of both the preferential orientation of the chains and the impeded diffusion through the surfactant layer. The alkyne, thus, can penetrate the surfactant layer, is transformed into the alkene on the surface, and if the hydrogen content at the surface is sufficiently large, can be further transformed into the alkane or isomerise. The latter explains the loss of selectivity at high hydrogen pressures. On the other hand, in the catalyst containing less ligand, the flattened HHDMA layer leaves only a few reaction pockets, where the alkyne molecules can adsorb and eventually react. Full selectivity can be retrieved when the comparative thermodynamic term for the adsorption of the alkyne is favourable with respect to that of the alkene (*i.e.*, strong alkyne and negligible alkene adsorption).[28–30] Since the reaction is carried out in solution, these adsorption energies have to be referenced to that of the solvent, as toluene or (cyclohexane) can competitively adsorb on the surface, acting as an additional selectivity modifier. We have computed these adsorption energies for 1-hexyne, 1-hexene, and toluene, employing the Pd-HHDMA model structure with the lowest ligand content. The resulting values (E_{ads} = −1.43, −0.45, −0.82 eV for 1-hexyne, 1-hexene, and toluene, respectively) indicate that, while 1-hexyne is strongly bound to the surface, 1-hexene can be easily displaced by the solvent, which further justifies the high alkene selectivity observed.

The catalytic results collected here apparently contrast with earlier works. Schwartz and co-workers, for example, observed, for thiol-decorated palladium and platinum nanoparticles, a decrease in activity with the increased thiol concentration.[13] This result, however, can be rationalised by comparing the HHDMA-covered nanoparticles with thiol- and amine-covered ones. While thiols and amines flatten on the surface independently from the ligand content,[31,32] the presence of anionic and cationic counterparts in the HHDMA ligand is responsible for the different ligand conformation at

low and high content. Thus, while thiols and amines can be displaced by the reactants,[33] which are strongly adsorbed on the surface, the same does not occur over HHDMA-modified nanoparticles. Similarly, Kiwi-Minsker and co-workers observed a 4-fold increase in the TOF of acetylene hydrogenation and a drop in olefin selectivity upon the removal of the ligand shell in PVP-protected Pd particles by UV-ozone irradiation.[6] This was attributed to the better accessibility of the reactants to the active sites. Also in this case, the nature of the interaction between these two classes of stabilisers (PVP and HHDMA) with the nanoparticles should be considered. PVP and HHDMA are chemically very different. PVP is a rather homogeneous polymer with internal covalent bonds, low polarity, two anchoring points (N and C═O bonds) and relatively small van der Waals contributions.[34] In contrast, HHDMA is a surfactant with charge separation (hydrophosphate anions and quaternary N cation heads), and a large van der Waals contributions due to the long aliphatic tails.[9] This produces an extra degree of freedom in the HHDMA-containing system, that allows the material to self-organise, behaving as a 2D material at low ligand coverages and as a 3D material at higher ligand coverages (Fig. 9a). This extra source of flexibility is the key factor that explains the differences between PVP and Pd-HHDMA catalyst.

Generalisation to other substrates

We have finally extrapolated the original findings to the hydrogenation of nitriles to amines and of carbonyls to alcohols. None of these applications has been previously studied over Pd-HHDMA/$TiSi_2O_6$. As shown in Fig. 11, the same activity pattern encountered in the case of alkynes has been obtained for these other functional groups. In particular, by increasing the ligand amount, an increased catalytic activity and a slightly decreased selectivity are observed. These findings further elucidate how hybrid catalysts can achieve full product selectivity for the hydrogenation of nitriles and carbonyls without typical additions of corrosive acids and/or toxic bases (*e.g.*, HCl and NH_3) in stoichiometric amounts and additional downstream separation steps. Thus, the electronic and geometrical modifications imparted by the ligand can efficiently limit the kinetics of undesired products formation.

Conclusions

We have prepared and characterised a series of HHDMA-modified Pd catalysts with different amounts of ligand. Advanced techniques going beyond state-of-the-art approaches were essential not only to visualise the changes in the thickness of the ligand shell on the Pd nanoparticles, but also to understand and describe its flexibility and structure. These techniques include high-resolution magic-angle spinning nuclear magnetic resonance spectroscopy, and transmission electron microscopy of the colloids after negatively staining with uranyl acetate. The materials were tested in the continuous-flow three-phase semi-hydrogenation of alkynes, evidencing an increased catalytic activity at higher ligand concentrations. DFT calculations enable to rationalise of this trend, showing that the adsorption geometry of HHDMA on Pd change upon decreasing the ligand amount. Particularly, the system passes from a 3D structure with an almost complete coverage of ligand, to a 2D structure at the lowest concentration, resembling that of the Lindlar catalyst. Moreover, it was found that the order parameter of the organic layer represents an important descriptor that governs the structure–activity relationships of these catalysts. These results were also generalised to the hydrogenation of other functional groups such as nitriles and carbonyls. Overall, our contribution has provided a deeper understanding of the influence of the HHDMA ligand on the catalytic performance of the hybrid catalysts. Despite having developed a new synthetic methodology to tune the ligand content in the material, the accurate quantification of the ligand coverage per nanoparticle remains an open question for future studies.

Acknowledgements

Financial support from ETH Zurich, ICIQ Foundation, and the Spanish Ministerio de Economía y Competitividad (CTQ2012-33826 and 'Ayuda formación Posdoctoral' Fellowship (N. A.-B.)) are acknowledged. Dr Roland Hauert (EMPA, Dubendorf) is acknowledged for the XPS analyses and Mr. Peter Tittmann for the help with catalyst preparation. The Scientific Centre for Optical and Electron Microscopy (ScopeM) of ETH is acknowledged for use of its facilities. BSC-RES is thanked for generous computational resources.

References

1 (*a*) A. Roucoux, J. Schulz and H. Patin, *Chem. Rev.*, 2002, **102**, 3757; (*b*) H.-U. Blaser, C. Malan, B. Pugin, F. Spindler, H. Steiner and M. Studer, *Adv. Synth. Catal.*, 2003, **345**, 1.

2 C. Burda, X. Chen, R. Narayanan and M. A. El-Sayed, *Chem. Rev.*, 2005, **105**, 1025.

3 (*a*) N. Semagina and L. Kiwi-Minsker, *Catal. Rev.: Sci. Eng.*, 2009, **51**, 147; (*b*) A. J. McCue, F. McKenna and J. A. Anderson, *Catal. Sci. Technol.*, 2015, **5**, 2449.

4 R. Venkatesan, M. H. G. Prechtl, J. D. Scholten, R. P. Pezzi, G. Machado and J. Dupont, *J. Mater. Chem.*, 2011, **21**, 3030.

5 H. Bönnemann, W. Brijoux, R. Brinkmann, E. Dinjus, T. Joussen and B. Korall, *Angew. Chem., Int. Ed. Engl.*, 1991, **30**, 1312.

6 M. Crespo-Quesada, J. M. Andanson, A. Yarulin, B. Lim, Y. Xia and L. Kiwi-Minsker, *Langmuir*, 2011, **27**, 7909.

7 P. T. Witte, P. H. Berben, S. Boland, E. H. Boymans, D. Vogt, J. W. Geus and J. G. Donkervoort, *Top. Catal.*, 2012, **55**, 505.

8 P. T. Witte, S. Boland, F. Kirby, R. van Maanen, B. F. Bleeker, D. A. M. de Winter, J. A. Post, J. W. Geus and P. H. Berben, *ChemCatChem*, 2013, **5**, 582.

9 G. Vilé, N. Almora-Barrios, S. Mitchell, N. López and J. Pérez-Ramírez, *Chem. – Eur. J.*, 2014, **20**, 5926.

10 G. Vilé, N. Almora-Barrios, N. López and J. Pérez-Ramírez, *ACS Catal.*, 2015, **5**, 3767.

11 E. H. Boymans, P. T. Witte and D. Vogt, *Catal. Sci. Technol.*, 2015, **5**, 176.

12 (*a*) P. A. Sheth, M. Neurock and C. M. Smith, *J. Phys. Chem. B*, 1996, **30**, 33; (*b*) P. A. Sheth, M. Neurock and C. M. Smith, *J. Phys. Chem. B*, 2005, **109**, 12449; (*c*) J. Greeley and M. Mavrikakis, *J. Phys. Chem. B*, 2005, **109**, 3460; (*d*) D. Teschner, J. Borsodi, A. Wootsch, Z. Révay, M. Hävecker, A. Knop-Gericke, S. D. Jackson and R. Schlögl, *Science*, 2008, **320**, 86; (*e*) A. J. McCue, C. J. McRitchie, A. M. Shepherd and J. A. Anderson, *J. Catal.*, 2014, **319**, 127; (*f*) A. J. McCue and J. A. Anderson, *Catal. Sci. Technol.*, 2014, **4**, 272; (*g*) A. J. McCue and J. A. Anderson, *Front. Chem. Sci. Eng.*, 2015, **9**, 142.

13 S. T. Marshall, M. O'Brien, B. Oetter, A. Corpuz, R. M. Richards, D. K. Schwartz and J. W. Medlin, *Nat. Mater.*, 2010, **9**, 853.

14 G. Fagherazzi, P. Canton, P. Riello, N. Pernicone, F. Pinna and M. Battagliarin, *Langmuir*, 2000, **16**, 4539.

15 (*a*) J. Schaefer, E. O. Stejskal and R. Buchdahl, *Macromolecules*, 1975, **8**, 291; (*b*) A. Pines, M. G. Gibby and J. S. Waugh, *Chem. Phys. Lett.*, 1972, **15**, 373; (*c*) B. M. Fung, A. K. Khitrin and K. Ermolaev, *J. Magn. Reson.*, 2000, **142**, 97.

16 G. Kresse and J. Furthmuller, *Phys. Rev. B: Condens. Matter Mater. Phys.*, 1996, **54**, 11169.

17 G. Kresse and J. Furthmuller, *Comput. Mater. Sci.*, 1996, **6**, 15.

18 G. Kresse and D. Joubert, *Phys. Rev. B: Condens. Matter Mater. Phys.*, 1999, **59**, 1758.

19 B. Hammer, L. B. Hansen and J. K. Nørskov, *Phys. Rev. B: Condens. Matter Mater. Phys.*, 1999, **59**, 7413.

20 S. Grimme, *J. Comput. Chem.*, 2006, **27**, 1787.

21 N. Almora-Barrios, G. Carchini, P. Błoński and N. López, *J. Chem. Theory Comput.*, 2014, **10**, 5002.

22 R. García-Muelas and N. López, *J. Phys. Chem. C*, 2014, **118**, 17531.

23 A. R. Leach, *Molecular Modelling Principles and Applications*, 2nd edn., 2001, p. 395.

24 F.-M. McKenna and J. A. Anderson, *J. Catal.*, 2011, **281**, 231.

25 (*a*) G. Nizri, S. Magdessi, J. Schmidt, Y. Cohen and Y. Talman, *Langmuir*, 2004, **20**, 4380; (*b*) Z. Lee, K.-J. Jeon, A. Date, R. Erni, T. J. Richardson, M. Frenklach and V. Radmilovic, *Nano Lett.*, 2009, **9**, 3365; (*c*) F. Schacher, E. Betthausen, A. Walther, H. Schmalz, D. V. Pevgushov and A. H. E. Müller, *ACS Nano*, 2009, **3**, 2095; (*d*) C. V. Synatschke, F. H. Schacher, M. Förtsch, M. Dreschsler and A. H. E. Müller, *Soft Matter*, 2011, **7**, 174.

26 J. C. Love, L. A. Estroff, J. K. Kriebel, R. G. Nuzzo and G. M. Whitesides, *Chem. Rev.*, 2005, **105**, 1103.

27 M. García-Mota, J. Gómez-Díaz, G. Novell-Leruth, C. Vargas-Fuentes, L. Bellarosa, B. Bridier, J. Pérez-Ramírez and N. López, *Theor. Chem. Acc.*, 2011, **128**, 663.

28 Y. Segura, N. López and J. Pérez-Ramírez, *J. Catal.*, 2007, **247**, 383.

29 F. Studt, F. Abild-Pedersen, T. Bligaard, R. Z. Sørensen, C. H. Christensen and J. K. Nørskov, *Science*, 2008, **320**, 1320.

30 J. A. Anderson, J. Mellor and R. P. K. Wells, *J. Catal.*, 2009, **261**, 208.

31 C. A. Schoenbaum, D. K. Schwartz and J. W. Medlin, *J. Catal.*, 2013, **303**, 92.

32 L. Altmann, S. Kunz and M. Bäumer, *J. Phys. Chem. C*, 2014, **118**, 8925.

33 M. M. Green, M. P. Reidy, R. D. Johnson, G. Darling, D. J. O'Leary and G. Willson, *J. Am. Chem. Soc.*, 1989, **111**, 6452.

34 M. Okumura, Y. Kitagawa, T. Kawakami and M. Haruta, *Chem. Phys. Lett.*, 2008, **459**, 133.